Angewandte Chemie International Edition

Angewandte International Edition Chemie

GDCh German Chemical Society

How to cite: *Angew. Chem. Int. Ed.* **2026**, 65, e23653
doi.org/10.1002/anie.202523653

RESEARCH ARTICLE

A Zincophilic and Negatively-Charged Self-Reconstructed Stratified Interface for Regulating Zn^{2+} Conduction and Nucleation Toward Conformal Dendrite-Free Deposition

Feng Yang[1] | Le Zhou[1] | Tianyu Zhang[2] | Hongfei Wang[1] | Chuqiao Xia[1] | Zhongqing Ma[3] | Yong Hu[2]

[1]Key Laboratory of the Ministry of Education for Advanced Catalysis Materials, Department of Chemistry, Zhejiang Normal University, Jinhua321004, P. R. China | [2]Institute of Nanocatalysis and Energy Conversion, College of Chemistry and Materials Engineering, Zhejiang A&F University, Hangzhou311300, P. R. China | [3]Bamboo Industry Institute, Zhejiang A&F University, Hangzhou, Zhejiang 311300, P. R. China

Correspondence: Hongfei Wang (whf0614@zjnu.edu.cn) | Zhongqing Ma (mazq@zafu.edu.cn) | Yong Hu (yonghu@zafu.edu.cn; yonghu@zjnu.edu.cn)

Received: 28 October 2025 | **Revised:** 3 February 2026 | **Accepted:** 11 February 2026

Keywords: $NaMgF_3$ | Na_3InF_6 | self-reconstructed stratified interface | zincophilicity | surface negativity

ABSTRACT

The practical deployment of aqueous Zn-ion batteries (ZIBs) is hindered by poor cycling stability, a consequence of dendrite growth and side reactions originating from irregular Zn nucleation and sluggish Zn^{2+} migration. Here, we construct a composite-phase $NaMgF_3/Na_3InF_6$ nanocube interphase (NMIF@Zn) that undergoes dynamic in situ reconstruction during plating into a stratified architecture. This transformation generates a zincophilic inner layer via preferential In^{3+} reduction, while the outer fluoride nanocubes retain a strong negative surface charge. The synergy between these reconstituted components and the nanocube matrix topology significantly enhances the interfacial electric double layer and creates unimpeded ion channels rich in zincophilic sites, collectively lowering the ion migration barrier and nucleation overpotential to enable conformal dendrite-free deposition. Consequently, the NMIF@Zn symmetric cell achieves superior cycling stability for 2000 h at 3 mA cm^{-2}/3 mAh cm^{-2}, along with stable operation at a high depth of discharge of 81.9%. When paired with a MnO_2 cathode, the interphase-optimized anode demonstrates excellent energy storage under high cathode loadings in both coin-type and pouch-cell configurations. This work establishes in situ interfacial conversion engineering as a powerful strategy to coordinately regulate ion flux and nucleation behavior, paving the way for durable Zn anodes in next-generation energy storage.

1 | Introduction

Growing safety concerns regarding energy storage technologies, driven by repeated incidents of fires and explosions in consumer electronics and grid-scale systems, have intensified the search for safer alternatives. Aqueous rechargeable batteries, recognized for their inherent non-flammability and high ionic conductivity, have thus emerged as promising successors to conventional Li-ion batteries (LIBs) [1, 2]. Among them, aqueous Zn-ion batteries (ZIBs) are particularly attractive due to Zn's material abundance, high energy density, and low cost [3, 4]. However, the practical application of Zn metal anodes faces significant challenges, such as dendrite growth, hydrogen evolution reaction (HER), and corrosion. These irreversible side reactions result in poor Coulombic efficiency (CE) and rapid capacity fade, underscoring the critical need to develop durable Zn anodes for the commercialization of ZIBs [5].

To date, extensive research efforts have been directed toward stabilizing the Zn anode through three primary strategies: electrolyte optimization [6, 7], separator design [8], and interface modification [9]. Electrolyte optimization, through methods

such as additive incorporation or concentration adjustment, can effectively regulate Zn^{2+} solvation and suppress side reactions. However, such strategies often face challenges, including high cost, limited environmental adaptability, and insufficient long-term interfacial stability under high-current conditions. While separator engineering focuses on homogenizing ion flux and physically blocking dendrites, it cannot fully prevent interfacial corrosion or provide nucleation guidance, leaving the anode partially unprotected. In contrast, constructing an artificial interface layer offers a more direct and structurally designable approach. This strategy not only shields the anode from electrolyte corrosion but also enables precise control over surface chemistry to guide uniform Zn nucleation and enhance ion transport. Importantly, such artificial interphases are compatible with existing electrode manufacturing processes, positioning them as one of the most readily commercializable pathways [10]. A variety of materials, including metals [11], inorganic compounds [12], organic polymers [13], and their composites [14], have been explored as functional interfacial layers. Despite considerable research, it remains highly challenging for a single interface layer to meet multiple requirements, particularly the coordinated regulation of Zn^{2+} conduction and nucleation. Electrically conductive metal interlayers (e.g., Sn [15], Cu [16], Ag [17], In [18]) have been reported to homogenize the electric field and provide abundant nucleation sites, thereby guiding uniform Zn deposition. However, such layers fail to prevent interfacial side reactions, as the deposited Zn remains in direct contact with the electrolyte, resulting in poor CE and limited reversibility. Additionally, although electronically insulating yet ion-conductive fluoride-based layers (e.g., ZnF_2 or related metal fluorides) can effectively regulate Zn^{2+} diffusion and confine Zn deposition beneath the coating, thereby suppressing dendrite formation [19]. Their performance as standalone artificial interphases is often constrained by practical interfacial limitations. These include interfacial contact resistance, restricted ion mobility in thick or dense layers, and limited stability during prolonged cycling, all of which can lead to significant polarization, particularly at high current densities [20–22]. Clearly, these single-component interfacial strategies each entail performance trade-offs, whether in unresolved side reactions or exacerbated polarization [23].

An effective protective layer for Zn anodes should feature high zincophilicity to guide nucleation, and superior cation conductivity [24]. The pursuit of a simple and feasible strategy to create such a multifunctional layer, which is crucial for realizing triple-free (dendrite-, HER-, and byproduct-free) Zn anodes, continues to be a highly compelling yet formidable goal in the field [25]. The judicious integration of zincophilic metals with inorganic fluoride coatings can offers a promising strategy to optimize anode/electrolyte interfacial chemistry [26]. In this context, a paradigm shift may come from leveraging the electric double layer (EDL), an inherent feature of the electrode/electrolyte interface, which could provide the breakthrough needed for substantial performance gains. By intentionally tailoring the anode interface layer to be more negatively charged, the interfacial Zn^{2+} concentration is increased, resulting in a stronger electric double layer capacitance (EDLC) and a relieved ion depletion [27]. Accordingly, an enhanced EDLC functions as a dynamic ion reservoir that not only facilitates rapid Zn^{2+} transport but also ensures uniform ion distribution, key to achieving stable, dendrite-free plating [28]. Given these insights, there is a compelling need to develop effective strategies for constructing metal/fluoride composite interlayers that can precisely modulate both zincophilicity and surface charge, while also deepening the fundamental understanding of their impact on Zn plating kinetics.

In this work, a protective layer of $NaMgF_3/Na_3InF_6$ nanocubes was constructed on the Zn electrode (denoted as NMIF@Zn). This layer spontaneously undergoes in situ self-reconfiguration into an In/fluoride stratified architecture during a galvanostatic charging process, thereby systematically regulating nucleation, mass transfer, and electrochemical reduction. The preferential reduction of In^{3+} forms a metallic In inner layer that offers abundant zincophilic sites, while the negatively charged fluoride nanocube outer surface enriches the interfacial Zn^{2+} concentration. Acting synergistically, the reconstituted components and nanocube matrix enhance the EDLC, accelerate Zn^{2+} migration, and reduce the nucleation barrier, collectively enabling conformal dendrite-free Zn deposition. As a result, the NMIF@Zn anode exhibits exceptional performance, including an extended plating/stripping cycling lifespan of 2000 h at 3 mA cm^{-2}/3 mAh cm^{-2} and robust stability at an 81.9% depth of discharge (DOD). Furthermore, NMIF@Zn//MnO_2 full cells achieve stable operation at a low N/P ratio of 1.5 in coin cells and deliver high energy density in pouch-cell configurations. This work thus presents a scalable and efficient in situ conversion strategy that induces a stratified interface with balanced zincophilicity and surface negativity, significantly enhancing the longevity of ZIBs and paving a promising route for their practical application.

2 | Results and Discussion

The performance of the NMIF@Zn anode was benchmarked against two control samples: a Zn electrode protected with $NaMgF_3$ nanocubes (NMF@Zn) and a bare Zn foil. Both modified electrodes were synthesized via a conventional spin-coating method. To overcome the intrinsic limitations of the bare Zn anode, the action mechanism of the NMIF interphase in optimizing interfacial electrochemical reactions is schematically presented in Figure 1a. The preferential reduction of In^{3+} during the initial electrodeposition stage drives the in situ formation of a uniquely stratified interface on the NMIF@Zn electrode. This self-reconstructed structure is distinctly bilayered: a metallic In inner layer acts as a zincophilic nucleation template, while an outer layer of fluoride nanocubes, endowed with intensified negative surface charges. This architecturally optimized interface addresses two fundamental challenges simultaneously. First, the negative surface charges on the fluoride nanocubes serve to enrich Zn^{2+} ions at the interface. This ion enrichment amplifies the EDLC, which effectively lowers the energy barrier for Zn^{2+} permeation through the interfacial layer, acting to enhance the overall ion transport kinetics. Second, the inner zincophilic In layer functions as a preferential host, offering abundant low-energy nucleation sites that guide homogeneous Zn deposition. This synergistically designed interface not only ensures a dendrite-suppressed anode but also optimizes the interfacial electrochemical environment, leading to markedly improved plating/stripping reversibility and enhanced structural integrity of the Zn anode during long-term cycling.

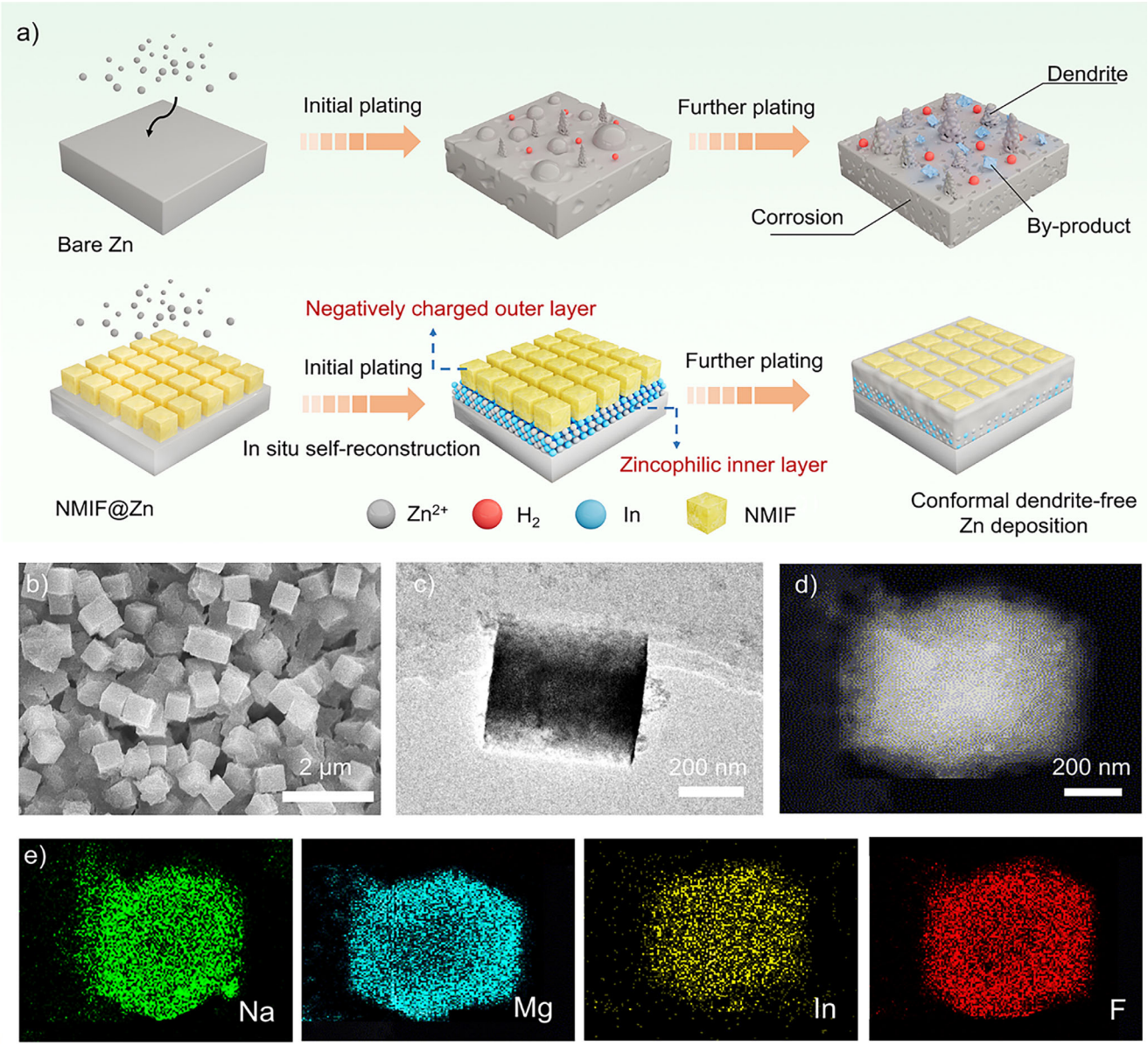

FIGURE 1 | a) Schematic diagram of the in situ self-reconstruction process on the NMIF@Zn anode, achieving a stratified coupling of a zincophilic inner layer and a negatively charged outer layer to enable conformal dendrite-free Zn deposition. b) SEM image and c) TEM image of the NMIF nanocubes. d) STEM and e) elemental mapping images of the Na, Mg, In, and F elements of a single NMMF nanocube.

The NMIF nanocubes were prepared by a straightforward co-precipitation approach. The phase identity of the product was determined by powder X-ray diffraction (XRD). The pattern presented in Figure S1 confirms the formation of a composite material characterized by two orthorhombic phases, identified as $NaMgF_3$ and Na_3InF_6, with no detectable crystalline impurities. The morphology and microstructure of the obtained NMIF were examined by scanning electron microscopy (SEM) and transmission electron microscopy (TEM). Representative images clearly show that the sample is composed of uniform nanocubes with smooth facets and an average size of about 400 nm (Figure 1b,c). This highly uniform cubic morphology suggests a homogeneous nucleation and growth process during synthesis. The sharp edges and smooth surfaces are indicative of high crystallinity, which is critical for its subsequent function as a stable interfacial layer. Scanning transmission electron microscopy (STEM) and the corresponding energy-dispersive X-ray spectroscopy (EDS) elemental mapping were performed to analyze the chemical composition. As shown in Figure 1d,e, the elements Na, Mg, In, and F are uniformly distributed throughout the entire architecture. This observed homogeneity at the nanoscale verifies the successful formation of a well-mixed composite, which is pivotal for ensuring consistent interfacial properties. Further insights into the surface chemistry were gained through X-ray photoelectron spectroscopy (XPS). The survey spectrum confirms the co-existence of Na, Mg, In, and F elements (Figure S2a). High-resolution analysis of the In 3d region in Figure S2b reveals doublet peaks located at binding energies of 446.2 eV (In $3d_{5/2}$) and 453.8 eV (In $3d_{3/2}$) [19]. The positions and spin-orbit splitting of these peaks are characteristic of In^{3+}, verifying that the In component retains its trivalent oxidation state within the composite structure, consistent with its presence in the Na_3InF_6 phase. To provide a

relevant morphological baseline for comparison, the NMF sample was characterized under identical conditions. The corresponding SEM image demonstrates that the NMF sample also adopts a nanocube structure (Figure S3). This morphological consistency between NMIF and NMF is critical for the comparative study, as it allows us to attribute differences in electrochemical performance primarily to the elemental composition and interfacial properties.

Herein, the NMIF nanocubes were prepared using a straightforward co-precipitation method conducted under ambient conditions, which offers strong potential for large-scale production due to its simplicity, low energy input, and compatibility with standard industrial processes [29]. The synthesis employs low-cost and commercially accessible precursors (NaF, $MgCl_2$, and $In(NO_3)_3$) in an aqueous medium, avoiding organic solvents, high temperatures, or controlled atmospheres. This room-temperature, one-step reaction is highly reproducible and yields uniform nanocubes (~400 nm) without the need for surfactants or complex templating agents. Moreover, the resulting NMIF dispersion can be readily deposited onto Zn substrates using common coating techniques such as spin-coating, blade-coating, or spray-coating, all of which align well with existing battery electrode manufacturing lines [30]. In this composite, the In content is optimized to achieve a balance between performance gains and material cost.

The thickness of the NMIF layer was tailored by adjusting the spin-coating time, yielding a series of NMIF@Zn electrodes for comparative study (Figure S4). Cross-sectional SEM analysis corroborates the presence of a uniform, continuous NMIF nanocube coating on the Zn substrate. The measured coating thickness is consistent with values from micrometer measurements (Figure S5), further confirming that the spin-coating method produces a homogeneous interfacial layer whose thickness can be effectively tuned by varying the coating time. Galvanostatic cycling of symmetric cells at increasing current densities from 1 to 10 mA cm^{-2} with a fixed capacity density of 1 mAh cm^{-2} was used to assess the rate performance of NMIF@Zn anodes with different coating thicknesses. As shown in Figure S6, the 20 µm-thick NMIF interfacial layer affords exceptional cycling stability with minimal polarization across all current densities. This optimal thickness likely offers a balanced combination of effective dendrite suppression and efficient ion transport. Deviations from this optimum, either a thinner (9 µm) or a thicker (32 µm) layer, lead to substantial voltage oscillations, suggestive of inadequate interfacial protection and increased ion diffusion resistance, respectively. The analysis of the desolvation energy based on Equation S1 further corroborates that a 20 µm NMIF layer is optimal (Figure S7). This specific thickness optimally lowers the desolvation energy barrier for hydrated Zn^{2+} ions, yet avoids the excessive Zn^{2+} transport resistance and associated concentration polarization that arise from an overly thick layer [31]. The fluoride-based nanocube layer is inherently hydrophobic, a property evidenced by the high water contact angle measured on the NMIF@Zn electrode surface (Figure S8). This hydrophobicity effectively repels water molecules from the immediate electrode/electrolyte interface. Consequently, the solvation sheath of the hydrated Zn^{2+} ions is weakened, which facilitates the removal of coordinated water. This pre-desolvation effect substantially lowers the energy barrier for the complete desolvation step before Zn deposition [26].

Another primary function of this design is to guide Zn deposition to conformally infill the 3D nanocube matrix, thereby suppressing vertical dendrite growth. This necessitates a coating with sufficient internal volume to accommodate the deposited metal. To validate this structural requirement, symmetric cells were tested under increasing areal capacities at 3 mA cm^{-2} (Figure S9). The 9 µm coating fails rapidly at 9 mAh cm^{-2}, as its limited thickness can not provide adequate space to guide deposition, leading to dendrite penetration. In contrast, the optimal 20 µm coating maintains stable operation even at a high capacity of 24 mAh cm^{-2} by offering sufficient volume for complete dendrite-free infilling. Meanwhile, the 32 µm coating, despite having ample volume, induces significant polarization at high capacities due to an increased ion transport distance, in agreement with its higher activation energy (E_a).

To further evaluate the stabilizing effect of the designed NMIF interfacial layer, symmetric cells were assembled using various modified electrodes and bare Zn foils. As depicted in Figure 2a, the symmetric cell with NMIF@Zn exhibits a long cycle life for 2000 h at 3 mA cm^{-2}/3 mAh cm^{-2}, outperforming the NMF@Zn (734 h) and bare Zn (50 h) counterparts. More importantly, the NMIF layer enables exceptional durability under practically relevant, harsh conditions. At a high current density of 20 mA cm^{-2} and a DOD of 33.3% (10 mAh cm^{-2}), the NMIF@Zn anode maintains stable operation for 1000 h (Figure 2b), substantially surpassing the reference cells. The outstanding performance stems from the unique properties of the NMIF layer, which successfully inhibits dendrite formation while promoting rapid ion conduction. To investigate the influence of the NMIF coating on Zn utilization, the symmetric cells were tested at a high DOD of 81.9% with an areal capacity of 24 mAh cm^{-2}, using a 50 µm-thick Zn foil [32]. As shown in Figure S10, the NMIF@Zn symmetric cell maintains stable operation for over 100 h under this demanding condition. This performance stands in stark contrast to the rapid failure of both the bare Zn and NMF@Zn cells, unequivocally demonstrating the superior protective efficacy of the NMIF coating. We also conducted control experiments by coating a slurry consisting of conductive carbon black and binder (without NMIF) onto a Zn foil to a comparable thickness. The symmetric cell with this carbon-coated anode exhibits rapid failure and large voltage fluctuations under under 1 mA cm^{-2}/1 mAh cm^{-2} (Figure S11), confirming that the carbon matrix alone cannot provide the necessary zincophilicity, negative surface charge regulation, or ion-transport pathways required for stable cycling. The rate performances of symmetric cells equipped with different electrodes are compared in Figure S12. Notably, the NMIF@Zn cell maintains exceptional cycling stability and exhibits the lowest voltage hysteresis across all tested current densities (Figure 2c). This reduced voltage hysteresis reflects the capability of the NMIF layer to enable rapid Zn^{2+} transport and sustain low polarization characteristics [33]. The exchange current density, derived from voltage hysteresis based on Equation S2, quantitatively confirms the superior kinetics of the NMIF@Zn electrode, which exhibits the highest value of 13.3 mA cm^{-2} (Figure S13). This result indicates the lowest energy barrier for Zn plating/stripping among the compared electrodes. Furthermore, benchmarking against previously reported systems establishes the superiority of this interfacial design (Figure 2d and Table S1) [34–44]. The well-engineered NMIF@Zn anode substantiates this conclusion by achieving an ultrahigh

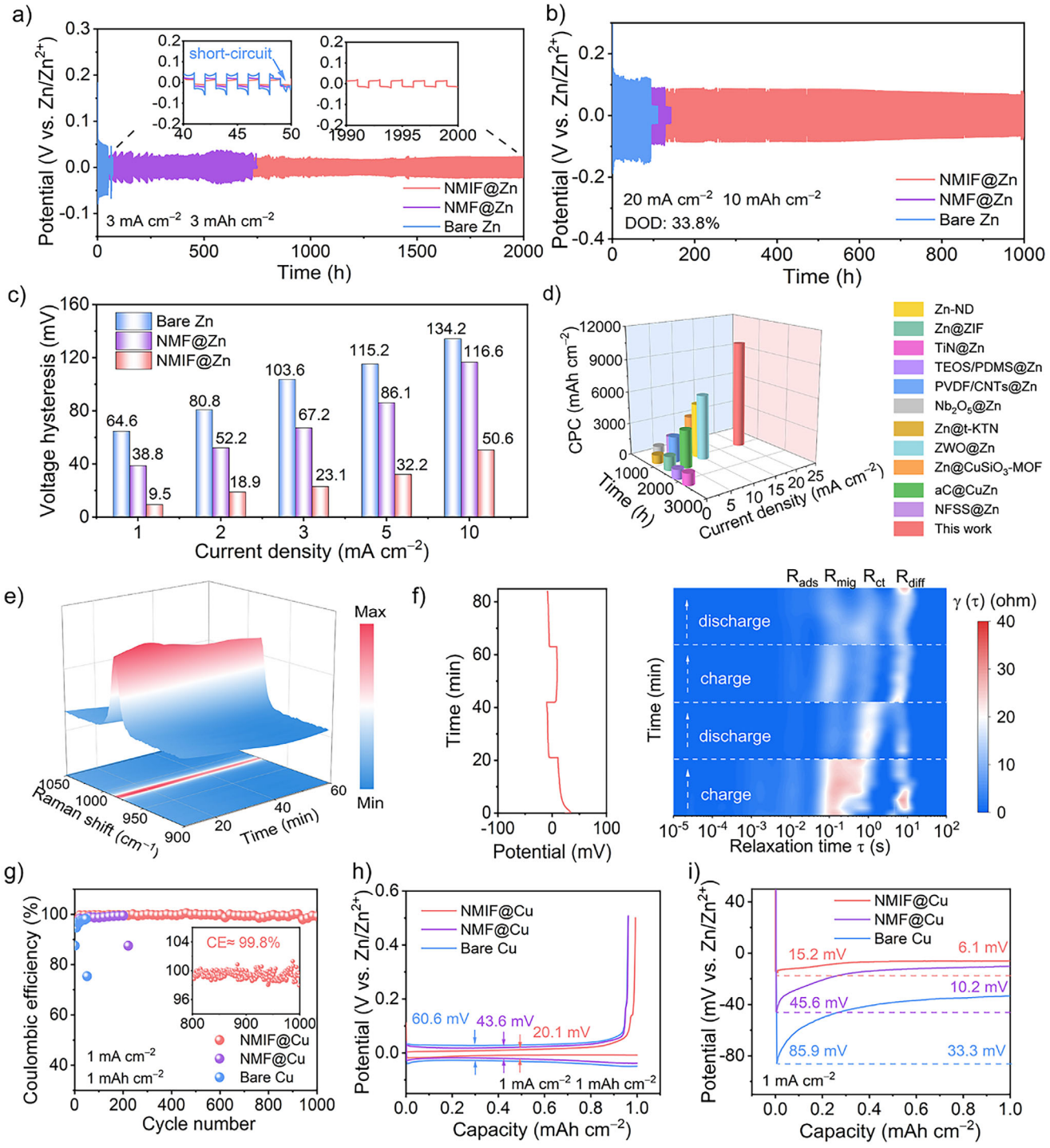

FIGURE 2 | Potential profiles of symmetric cells using different electrodes at a) 3 mA cm^{-2}/3 mAh cm^{-2} and b) 20 mA cm^{-2}/10 mAh cm^{-2}. c) Voltage hysteresis of symmetric cells at different current densities. d) CPC and cycling lifespan of the NMIF@Zn anode compared with other reported works. e) In situ Raman characterization during the Zn plating process for the NMIF@Zn electrode. f) In situ DRT of the NMIF@Zn//NMIF@Zn cells for two consecutive plating/stripping cycles. g) CE measurements of asymmetric cells with different electrodes at 1 mA cm^{-2}/1 mAh cm^{-2} and h) comparison of corresponding potential profiles at the 10th cycle. i) Zn deposition curves at 1 mA cm^{-2}.

cumulative plating capacity (CPC) of 10 Ah cm^{-2} under a high current density.

Interfacial mass transport properties further attest to the improved Zn deposition kinetics. The Zn^{2+} concentration dynamics were interrogated by in situ Raman spectroscopy, targeting the SO_4^{2-} vibration band (984 cm^{-1}). A stark spatial gradient in Zn^{2+} emerges within 20 min near bare Zn and NMF@Zn electrodes (Figure S14), signaling non-uniform electrodeposition. Conversely, the NMIF-modified anode preserves an exceptionally homogeneous Zn^{2+} distribution throughout plating (Figure 2e), attesting to its efficacy in regulating ion transport. To gain

deeper insight into the electrochemical relaxation dynamics, we employed in situ electrochemical impedance spectra (EIS) coupled with distribution of relaxation times (DRT) analysis on symmetric cells (Figure S15). The DRT analysis resolves four distinct relaxation processes: Zn^{2+} diffusion resistance (R_{diff}, $\tau \approx 10^1$ s) corresponding to the diffusion of Zn^{2+} and $[Zn(H_2O)_6]^{2+}$ species; charge transfer resistance (R_{ct}, $\tau \approx 10^0$ s); surface migration resistance (R_{mig}, $\tau \approx 10^{-1}$ s), associated with Zn^{2+}/Zn migration on the electrode surface and subsequent formation of Zn crystals; and adsorption resistance (R_{ad}, $\tau \approx 10^{-2}$ s), reflecting the adsorption and desolvation processes of $[Zn(H_2O)_6]^{2+}$ at the electrode/electrolyte interface [45–48]. The evolution of the DRT peaks reflects the dynamic changes in interfacial processes during cycling (Figure 2f). In the first Zn deposition step, the R_{mig} and R_{ct} are relatively high, which can be attributed to the pre-reduction of In^{3+} and the resulting in situ interfacial restructuring at the NMIF@Zn electrode. This multi-step redox process contributes to higher overall interfacial resistances. After a complete initial charge/discharge cycle, a stable interface is formed. Supported by the synergistic modulation from the zincophilic In layer and the negatively charged fluoride nanocube, the DRT data from the second cycle confirm stable Zn^{2+} diffusion and migration, as well as consistent Zn nucleation and growth processes at the interface.

The CE value was further tested in asymmetric cells to quantify the reversibility of Zn plating/stripping. CE tests were conducted using an NMIF-modified Cu electrode as the working electrode and a bare Zn foil as both the counter and reference electrode. This approach avoids interference from the underlying Zn source, thereby allowing for a more accurate examination of the CE during Zn plating/stripping [49, 50]. The measurements were performed at lower current densities of 1 mA cm^{-2} (with a fixed areal capacity of 1 mAh cm^{-2}) to more sensitively evaluate the impact of interface modification on the reversibility of Zn deposition/stripping. The NMIF@Cu electrode maintains stable cycling while achieving a high average CE of 99.8% over 1000 cycles at 1 mA cm^{-2} (Figure 2g), substantially outperforming the bare Cu electrode and NMF-modified Cu electrode, which fail rapidly due to severe side reactions and inhomogeneous deposition. In addition, the CE was quantified by performing the modified Aurbach's method in Zn//Cu cell configurations. A key preparatory step involved pre-depositing an excess Zn reservoir at a current density of 1 mA cm^{-2} with an areal capacity of 5 mAh cm^{-2} onto the Cu working electrode before cycling to establish a stable baseline and minimize nucleation effects. Following galvanostatic cycling at 1 mA cm^{-2} and 1 mAh cm^{-2} (Figure S16), the Zn//NMIF@Cu cell achieves a high average CE of 96.2%, which is higher than that of the Zn//NMF@Cu cell (94.1%). The Zn//Cu control cell, however, experiences early failure caused by irreversible dendrites and side reactions [51]. This improvement demonstrates that the in situ reconstructed NMIF interface substantially enhances the reversibility of Zn plating/stripping, underscoring its critical role in stabilizing the Zn anode electrochemistry. Further analysis of the potential profiles in Figure 2h demonstrates the kinetic superiority of the NMIF@Zn electrode, which exhibits a significantly lower overpotential (20.1 mV) than its counterparts (43.6 mV for NMF@Zn and 60.6 mV for bare Zn). Critically, the NMIF@Zn electrode also maintains an exceptionally stable voltage hysteresis with highly reproducible plateaus over multiple cycles (Figure S17), signaling a stable and reversible electrochemical interface. The minimal polarization and its exceptional stability collectively point to a well-regulated ion flux and stable deposition behavior. Analysis of the anodic polarization curves identifies the nucleation overpotential, indicative of initial deposition kinetics, and the plateau overpotential, dominated by Zn^{2+} diffusion (Figure 2i). Notably, the NMIF@Zn electrode exhibits a unique activation and self-optimization behavior, with a marked decrease in both overpotentials after the first cycle (Figure S18). This suggests a dynamic interfacial reconfiguration that permanently enhances subsequent deposition kinetics. In its stabilized state, the NMIF@Zn electrode requires a nucleation overpotential of only 15.2 mV (vs. 45.6 mV for NMF@Zn and 70.5 mV for bare Zn) and a plateau overpotential of merely 6.1 mV (vs. 10.2 mV for NMF@Zn and 32.6 mV for bare Zn) at 1 mA cm^{-2}.

Based on the enhanced Zn deposition kinetics and stability provided by the NMIF coating, as demonstrated by electrochemical tests, the relationship between the structure of the interfacial layer and the deposition behavior was further investigated through theoretical calculations and experimental characterization. To probe the origin of the enhanced interface stability, density functional theory (DFT) calculations were conducted to analyze the differential charge density of NMIF@Zn. The result reveals pronounced charge transfer at the interface (Figure S19), confirming a strong electronic interaction between the NMIF layer and the Zn substrate. This interaction is critical for reinforcing interfacial adhesion and promoting efficient charge transfer, thereby synergistically accelerating electrochemical kinetics. The adhesion between the coating and the Zn substrate was further evaluated by immersing NMIF@Zn and NMF@Zn electrodes in hot water at 93°C for 10 min (Figure S20). Post-treatment cross-sectional SEM analysis reveals that both coatings maintain intimate contact with the substrate, showing no interfacial gaps, cracks, or delamination (Figure S21). This confirms that such metal-fluoride nanocube coatings in general exhibit inherently good adhesion to Zn surfaces, which is beneficial for their application as protective interlayers. To directly probe the interfacial electronic interaction and adhesion between the NMIF coating and the Zn substrate, additional high-resolution XPS analysis was further performed on the NMIF coating, bare Zn foil, and the as-prepared NMIF@Zn electrode before any electrochemical cycling. All XPS spectra were recalibrated using the adventitious C 1s peak at 284.8 eV as an internal reference (Figure S22). The comparative XPS results reveal a clear charge redistribution at the interface. The Zn 2p peaks in the NMIF@Zn sample shift to a higher binding energy compared to those in bare Zn foil, while concurrently, the F 1s peak from the fluoride component in NMIF@Zn shifts to a lower binding energy relative to its position in the pristine NMIF powder (Figure S23). The increase in Zn binding energy indicates electron donation from the Zn substrate, whereas the decrease in F binding energy signifies that F accepts electron density.

The observed decrease in nucleation overpotential during the initial cycles of the NMIF@Zn electrode points to dynamic interfacial evolution. Driven by the more positive standard electrode potential of In^{3+}/In compared to Zn^{2+}/Zn, the In species in the NMIF interfacial layer is thermodynamically favored to reduce first, forming a metallic In phase. This process is not limited by the initial spatial distribution because the reduction occurs dynamically at the electrode/electrolyte interface, where In^{3+}

ions can migrate to active reduction sites. This precursor reaction fundamentally alters the electrochemical interface, guiding the subsequent Zn nucleation toward a more uniform and kinetically favorable deposition process. Providing experimental evidence for the above assertion, the NMIF layer was removed from the plated NMIF@Zn electrode for phase analysis. Subsequent SEM and EDS mapping images of the exposed Zn substrate reveal a highly homogeneous spatial distribution of In across the surface (Figure S24). This confirms that In^{3+} ions, uniformly released from the NMIF coating, are homogeneously reduced across the electrode surface, forming a continuous In-rich interfacial film. To elucidate the depth-dependent chemical states of the electroplated interface (1 mA cm^{-2} for 1 h), we performed high-resolution XPS profiling on the NMIF@Zn electrode with the fluoride layer removed after sequential Ar^+ etching (0, 100, 200, and 300 s). The Zn 2p binding energy shifts upward by 0.2 eV (from 1022.4/1045.4 eV to 1022.6/1045.6 eV) as the etching time increases from the initial stage to 300 s (Figure 3a). Concurrently, a peak deconvolution analysis was carefully conducted on the In 3d spectra obtained at different Ar^+ etching times [19]. As clearly shown in Figure 3b, a gradual evolution in the In 3d spectra is observed with increasing sputtering depth, where the electronic state of the pre-reduced In changes progressively. This spectral change can be attributed to the strong interfacial interaction between In and neighboring Zn atoms, leading to the formation of a unique interfacial phase [52]. The dominance of the In^0 signal at the surface can be understood through our proposed mechanism. First, a metallic In layer forms in situ at the interface during the initial plating stage. Subsequently, Zn deposits beneath and interacts with this In layer. Consequently, when the top coating is removed for analysis, the In-rich interfacial region becomes the outermost surface, resulting in the strong In^0 signal observed at the start of the depth profile [53]. This result indicates strong electronic interaction and likely the formation of a Zn-In interface. The XPS spectra also show a minor In^{3+} component. This signal originates from the surface oxidation of metallic In upon air exposure during sample transfer for *ex-situ* analysis. Comparative XRD analysis was further performed on the plated NMIF@Zn electrode after removal of the NMIF coating alongside a bare Zn foil reference (Figure S25). The XRD pattern of the NMIF@Zn electrode exhibits clear shifts in the positions of the Zn diffraction peaks compared to bare Zn. Specifically, the Zn (002) peak shifts from $2\theta = 36.20°$ (bare Zn) to 36.06° (NMIF@Zn), and the Zn (101) peak shifts from $2\theta = 38.90°$ (bare Zn) to 38.75° (NMIF@Zn). These systematic peak shifts indicate lattice expansion due to the incorporation of In atoms into the Zn matrix. Such expansion is consistent with the interfacial incorporation of In atoms into the Zn matrix, resulting in the formation of a modified interfacial region with distinct structural parameters [54–56]. The significantly stronger adsorption of a Zn atom on the In slab (−1.48 eV) compared to on the Zn slab (−0.52 eV) confirms its function as a highly efficient zincophilic mediator for Zn deposition (Figure 3c). This high zincophilicity means the In layer provides abundant low-energy sites for Zn nucleation. Consequently, it functions not as a dense barrier, but as a guiding scaffold that promotes uniform Zn deposition on and within its matrix. The longitudinal gradient of In and Zn in the plated NMIF@Zn anode (with NMIF layer removed, Figure 3d) was investigated by time-of-flight secondary ion mass spectrometry (TOF-SIMS). Depth profiling was conducted via O_2^+ sputtering, monitoring In^+ and Zn^+ fragments. After the initial influence from residual coating diminishes, the ion signals stabilize with deeper etching (Figure 3e). It is possible that trace residues of the fluoride-rich coating remained on the topmost surface. These residues could contribute to the initial In signal, leading to a relatively higher intensity at the very beginning of the sputtering process. The stabilization of these signals directly validates the efficacy of the pre-reduction strategy in forming a metallic In layer within the Zn deposit. The TOF-SIMS analysis reveals a graded and intermixed distribution of In and Zn, suggesting the pre-reduced In forms a nanoscale and discontinuous layer that guides deposition rather than forming a solid-state diffusion barrier. Thus, Zn^{2+} ions can readily migrate through the boundaries or defects in this nanoscale layer.

Complementing the inner zincophilic layer, the physicochemical properties of the outer fluoride nanocube layer were also examined. DFT calculations demonstrate that the reduction of In^{3+} induces a pronounced broadening and partial filling of the projected density of states (PDOS) for F near the Fermi level (Figure S26). This electronic redistribution signifies a delocalization of electron states and a concurrent increase in the overall negative charge on F. This electron redistribution was further investigated by examining the topology of the electron density, complemented by an analysis of the electron localization function (ELF). The side view of the ELF visualizes the effect of the In defect formation, which is manifested as a pronounced enhancement of electron delocalization into the F region (Figure 3f). The XPS analysis at various plating capacities shows that the atomic percentage of In within the coating remains virtually unchanged after the initial period (Figure S27). This unambiguously demonstrates that the conversion reaction is self-terminating. Once the In/fluoride-modified interface is established, it passivates the underlying NMIF. Further plating/stripping cycles then proceed via the reversible deposition/dissolution of Zn onto/from this stable interface. Zeta potential measurements reveal a significant increase in surface negativity for NMIF@Zn (from −3.76 mV to −9.22 mV) after treatment at the reduction potential in a Na_2SO_4 solution (Figure S28). This value is also more negative than those of NMF@Zn (−0.65 mV) and bare Zn (0.83 mV). The enhanced negative charge at the interface is expected to promote Zn^{2+} adsorption while repelling SO_4^{2-} anions, thereby effectively modulating the EDL structure and optimizing the transport and deposition kinetics of Zn^{2+} ions. The EDLC values, derived from CV tests at various sweep rates (Figure 3g and Figure S29), correlate with the interfacial reaction kinetics. The NMIF@Zn electrode exhibits a significantly higher EDLC value (7.31 mF cm^{-2}) than the NMF@Zn (2.19 mF cm^{-2}) and bare Zn (0.13 mF cm^{-2}), confirming a greater concentration of Zn^{2+} ions within the compact layer near the interface. As illustrated in Figure 3h, the synergistic effect between the negatively charged fluoride nanocube and the pre-reduced In layer reconstructs the EDL, thereby establishing a steeper potential gradient and a higher local Zn^{2+} concentration, which collectively enhance the interfacial reaction kinetics [57]. The key interfacial electrochemical process involves a cation exchange-coupled reduction mechanism, which can be summarized by the following consolidated reaction equation during the initial plating stage:

$$Na_3InF_6 + xZn^{2+} + (3+2x)\,e^- \rightarrow In + 3Na^+ + xZnF_2 \cdot (1-x)\,Na_3InF_6$$

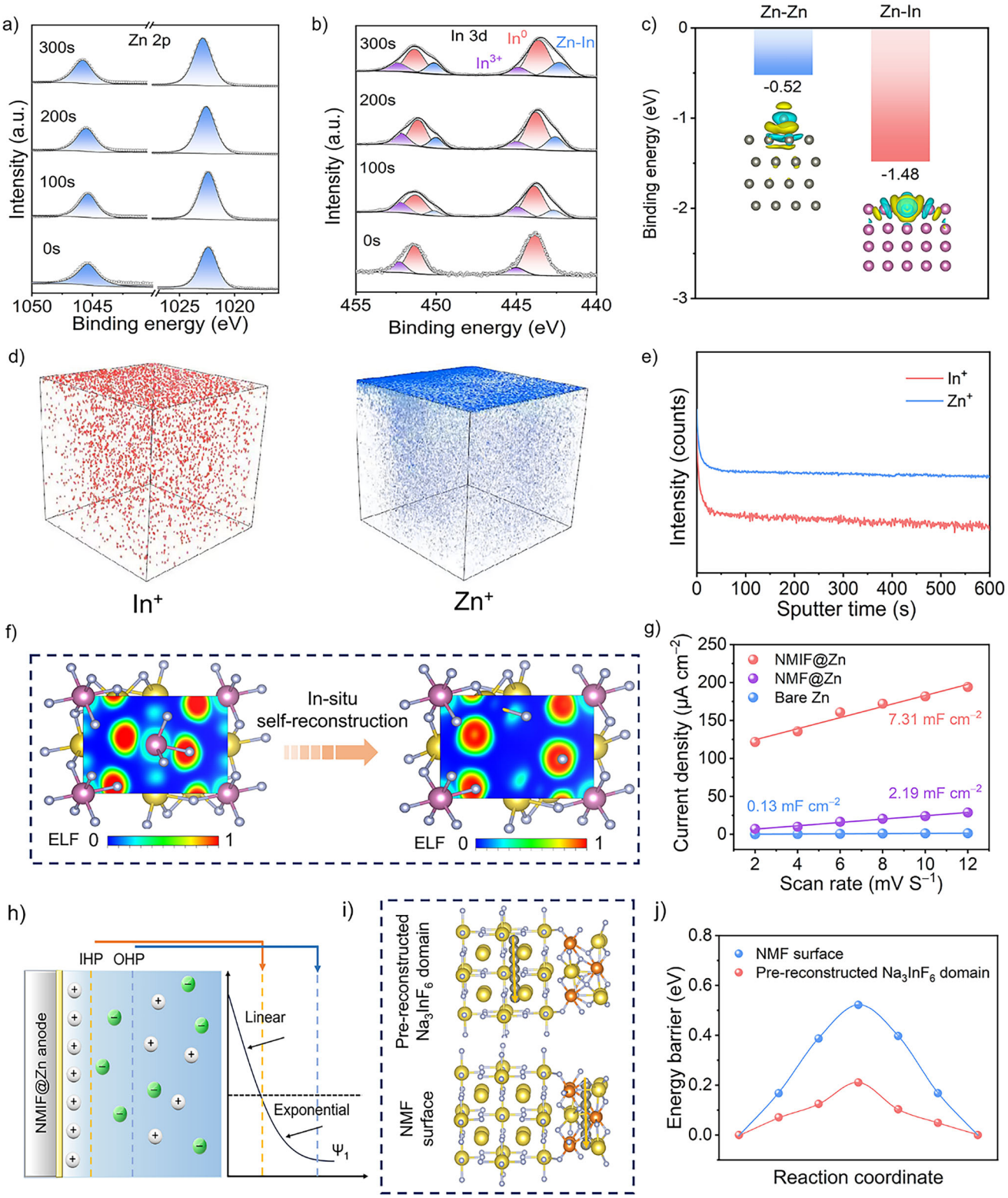

FIGURE 3 | High-resolution a) Zn 2p and b) In 3d XPS spectra of the NMIF@Zn electrode at different Ar^+ etching times. c) Optimized structures, charge density differences, and the corresponding binding energies of Zn adsorbed on the surfaces of In and Zn slabs. TOF-SIMS analysis of the reconstructed NMIF@Zn electrode after NMIF layer removal. d) 3D reconstruction revealing the spatial intermixing and architectural evolution of In^+ (red) and Zn^+ (blue) secondary ions. e) Corresponding depth profiles illustrating the distribution of In and Zn as a function of sputtering time. f) Side-view ELF of NMIF@Zn before and after interfacial reconstruction. g) EDLC values of NMIF@Zn, NMF@Zn, and bare Zn electrodes. h) Schematic of the EDL structure of NMIF@Zn with a reinforced Zn^{2+} concentration. i) Zn^{2+} diffusion pathways and j) migration energy barriers for the NMF surface vs. the pre-reconstructed Na_3InF_6 domain within the NMIF system.

This mechanism proceeds through two synergistic steps. First, due to its more positive redox potential, In^{3+} from the Na_3InF_6 component is preferentially reduced to form the metallic In inner layer. Concurrently, to compensate for the charge and structural vacancies created by this reduction, Zn^{2+} ions from the electrolyte migrate into the fluoride lattice, forming Zn–F bonds and stabilizing the anionic framework. Meanwhile, the $NaMgF_3$ phase remains electrochemically inert, serving as a stable and structural scaffold that supports the composite matrix. The transient Na^+ ions released during the very initial nucleation step may play a beneficial role. These cations can function as an electrostatic shield to homogenize the localized electric field, thereby suppressing dendrite initiation [58, 59]. DFT calculations in Figure 3i,j reveal a markedly lower migration energy barrier for Zn^{2+} ions across the pre-reconstructed Na_3InF_6 domains (0.21 eV) compared to the pure $NaMgF_3$ surface (0.52 eV). This confirms that the pre-reduction of In^{3+} not only creates zincophilic sites but also electronically modifies the local fluoride structure, creating pathways with lower ion diffusion barriers, as visually demonstrated in Figure S30. Consequently, it delays the onset of interfacial impoverishment and promotes uniform Zn electrodeposition. The measurement entailed the assembly of Zn//NMIF@Cu, Zn//NMF@Cu, and Zn//Cu asymmetric cells, with subsequent CV conducted at various scan rates. The Zn^{2+} diffusion coefficient ($D_{Zn}{}^{2+}$) was then calculated from the peak currents using the Randles-Sevcik equation, which is a standard and suitable method for evaluating interfacial ion transport kinetics. The reconstructed NMIF interface exhibits superior Zn^{2+} diffusivity, with the highest measured diffusion coefficient of 2.29 $\times 10^{-4}$ cm^2 s^{-1} (Figure S31), validating its key role in enhancing interfacial ion transport kinetics [60, 61]. To further bridge the theoretical models with the real interfacial architecture, we have supplemented the study with cross-sectional SEM (Figure S32) and elemental mapping performed on an NMIF-coated Cu foil electrode after electrochemical reconstruction (the Cu substrate was used to avoid interference from the Zn substrate during the deposition analysis). The results reveal the formation of an In-rich layer at the interface between the coating and the substrate, while Na, Mg, and F remain uniformly distributed within the coating matrix (Figure S33). Furthermore, Zn is observed not only within the coating but also overlapping with the In layer, indicating that Zn^{2+} ions permeate the coating and coexist with the pre-reduced In. The Na_3InF_6 component acts as the active moiety. During initial plating, In^{3+} is preferentially reduced to metallic In, forming a zincophilic inner layer. This reduction simultaneously enhances the negative surface charge across the fluoride matrix, promoting interfacial Zn^{2+} enrichment and significantly boosting the EDLC. In contrast, the $NaMgF_3$ phase remains electrochemically inert, serving as a stable structural scaffold that maintains the integrity of the 3D nanocube framework. It provides mechanical support and defines the microchannels that guide Zn deposition. Its ordered structure, synergizing with the negatively charged surface derived from the reconstructed Na_3InF_6 domains, facilitates efficient ion transport. Chronoamperometry (CA) was employed to investigate the Zn^{2+} diffusion dynamics during the nucleation and growth phase. For the NMIF@Zn anode (Figure S34), the current rapidly reaches a steady state at 20.9 mA cm^{-2} after a short transient, signifying a quick shift from 2D surface diffusion to stable 3D diffusion-controlled growth. This signifies that Zn^0 adatoms, produced from the reduction of Zn^{2+} ions that have passed through the fluoride layer, are efficiently captured by the zincophilic In sites. The excellent zincophilicity of In restricts random surface migration, curbing 2D diffusion. Conversely, prolonged 2D diffusion is more prevalent on NMF@Zn and bare Zn anodes, which originates from the lack of such efficient confinement and results in uneven deposition.

SEM characterization was performed to track the morphological evolution of Zn deposition on the NMIF@Zn substrate under operando conditions. At a current density of 1 mA cm^{-2} and a deposition capacity of 1 mAh cm^{-2} (Figure 4a), the gaps between NMIF cubes were preferentially filled with electrodeposited Zn. This behavior results the pre-reduced In layer, which forms a zincophilic interface that directs initial nucleation to the cube surfaces, thereby promoting lateral growth within the 3D framework. This mechanism allows the plated Zn to fuse and homogeneously infill the modified layer without dendrite formation, even at a high capacity of 3 mAh cm^{-2}. In contrast, under the same conditions, the NMF@Zn and bare Zn anodes (Figure 4b,c) developed disordered dendrites and protrusions by 2 mAh cm^{-2}. At 3 mAh cm^{-2}, these control electrodes were dominated by large, plate-like deposits, while the NMIF@Zn surface instead exhibits progressive smoothing, which effectively prevents vertical overgrowth. Surface roughness analysis via confocal laser scanning microscopy (CLSM) further demonstrates a more homogeneous surface morphology of the NMIF@Zn electrode after 50 cycles at 1 mA cm^{-2}, in stark contrast to the cycled NMF@Zn and bare Zn electrodes (Figure S35). The observed surface improvement originates from a conformal Zn deposition onto the nanocube structure, which effectively lowers the thermodynamic driving force for dendritic nucleation and growth. These electrochemical morphological features are directly corroborated by real-time in situ optical microscopy performed at 10 mA cm^{-2} (Figure S36). As anticipated, the engineered NMIF@Zn electrode maintains exceptional stability, with its surface remaining completely free of irregularities or dendritic protrusions throughout the plating process. In sharp contrast, severe surface roughening and dendritic growth emerge on the bare Zn foil within merely 20 min. *Ex situ* SEM and corresponding EDS mapping were conducted on the NMIF@Zn electrode after 100 cycles at 3 mA cm^{-2}. As shown in Figure S37, the nanocube morphology of the fluoride layer is well-preserved, with no signs of delamination or structural collapse. Furthermore, the EDS mapping confirms that the elements F, Na, and Mg remain uniformly distributed across the surface, indicating that the composite layer maintains its structural integrity and does not detach. The fact that In is distributed across the entire electrode surface suggests that pre-reduction has occurred. To probe the interfacial stability conferred by this process, cross-sectional SEM analysis was therefore conducted. As presented in Figure S38, the interfacial layer remains intact and well-adhered to the Zn substrate after cycling. Importantly, the thickness of the NMIF-based interphase shows no obvious change compared to the as-prepared state, indicating its structural stability during the electrochemical reconstruction and long-term cycling. To further probe the chemical stability of the interfacial components, we conducted XPS depth profiling on the cycled NMIF@Zn anode (after 100 cycles). The high-resolution F 1s spectra at different etching times (0, 100, 200, and 300 s) consistently show the presence of metal–F bonds, and the F content remains stable throughout the depth (Figure S39). This confirms that the fluoride-based outer layer is not only present but also chemically stable after repeated plating/stripping. Linear

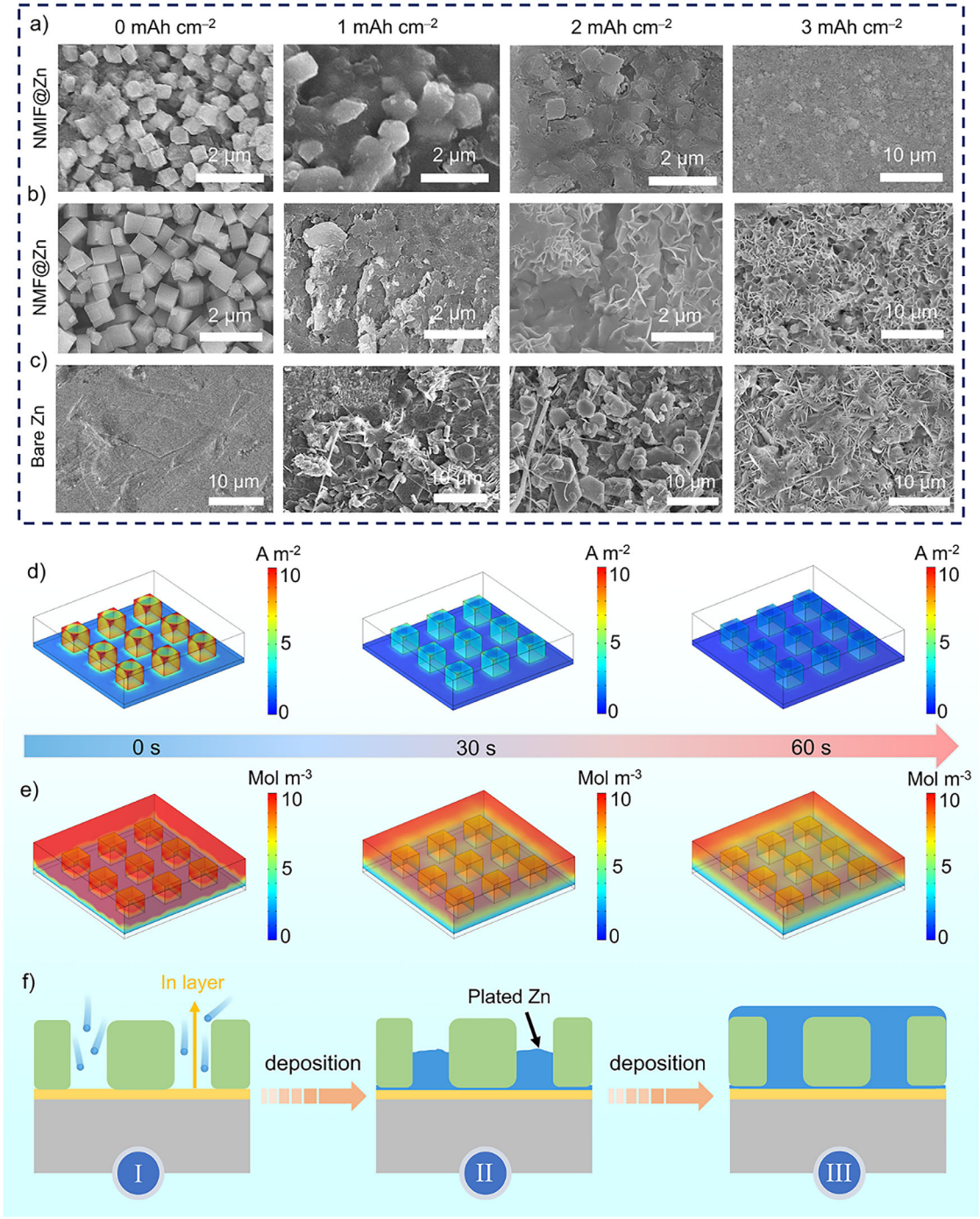

FIGURE 4 | SEM images of the a) NMIF@Zn, b) NMF@Zn, and c) bare Zn electrodes after Zn deposition at different areal capacities. Finite element simulation of the d) current density and e) Zn^{2+} concentration distribution on the NMIF@Zn electrode. f) Schematic illustration of the Zn deposition mechanism on the NMIF@Zn electrode.

polarization was employed to compare the corrosion behaviors of bare Zn, NMF@Zn, and NMIF@Zn electrodes (Figure S40). The results show that NMIF@Zn has the highest corrosion potential and the lowest corrosion current density, correlating with its significantly enhanced corrosion resistance. This confirms the protective nature of the NMIF interface in mitigating parasitic side reactions. Besides, the asymmetry observed in the Tafel plot for bare Zn may be attributed to the irreversible surface degradation and dynamic corrosion processes occurring during the anodic polarization scan, which prevent the establishment of a steady state. The more symmetric curve for NMIF@Zn indicates effective interfacial stabilization [62]. To assess the ability of the HER suppression, linear sweep voltammetry (LSV) was performed. As displayed in Figure S41, the NMIF@Zn electrode shows an HER onset potential of −1.133 V at 10 mA cm^{-2}, which is shifted negatively compared to those of NMF@Zn (−1.075 V) and bare Zn (−1.064 V), confirming the effective HER inhibition afforded by the NMIF layer.

Given that ion concentration and electric field distributions are critical for uniform Zn^{2+} deposition, we performed finite element simulations to compare these parameters on the NMIF@Zn and bare Zn surfaces. This theoretical investigation provides a basis for understanding how the NMIF interfacial reconstruction regulates Zn deposition behavior. Finite element simulations in Figure S42 reveal an inhomogeneous current density distribution on bare Zn, with the highest intensity localized at protrusion tips. This coupled interaction between the concentrated current and depleted ions further accelerates non-uniform deposition, thereby establishing a self-amplifying cycle that ultimately leads to dendritic growth. The dynamic simulations of current density and Zn^{2+} concentration distribution on the NMIF@Zn electrode are presented in Figure 4d,e. Initially, an ultrahigh current density accumulates on the nanocube surfaces, which is attributed to their enhanced negative charge after pre-reduction. This current density then continuously decreases with plating time, a phenomenon consistent with an over-limiting current behavior within the microchannels [63]. This temporal evolution suggests that Zn^{2+} ions are preferentially deposited in the microchannels formed by the pre-reduced In layer and fluoride nanocubes. After 60 s of plating, the current density distribution becomes significantly more uniform compared to the initial state. Concurrent with the current evolution, the Zn^{2+} concentration in the microchannels exhibits a gradual depletion before homogenizing. This spatial-temporal profile indicates that initial nucleation is preferentially guided by the zincophilic In layer, thereby initiating deposition within the fluoride matrix. Subsequent infilling of the microchannels with metallic Zn flattens the electrode topography and uniformizes the interfacial Zn^{2+} flux, ultimately resulting in stable deposition. The electric field and ion concentration profiles, revealed by finite element simulations, show that during plating, the current density and Zn^{2+} flux are concentrated within these microchannels. This directs the initial Zn nucleation to occur preferentially at the zincophilic In layer located at the bottom of these gaps, rather than on the top surface of the coating. Once nucleated, the deposited Zn grows laterally to fill the microchannels from the substrate upward, progressively "healing" the gaps. The overlying nanocube framework acts as a physical guide, constraining vertical growth and promoting lateral expansion, thereby yielding a dense, conformal Zn layer beneath the coating.

Based on the collective evidence, we propose that the in situ interfacial reconstruction enabled by the NMIF nanocube layer significantly enhances the operational longevity of the Zn anode. As schematically illustrated in Figure 4f, the Zn plating process on NMIF@Zn can be delineated into three consecutive stages: (i) During the initial discharge, In^{3+} ions from the fluoride nanocubes are preferentially reduced to form a metallic In layer on the substrate, owing to the more positive redox potential of In^{3+}/In compared to Zn^{2+}/Zn. (ii) This in situ-formed, zincophilic In layer then guides the uniform nucleation of Zn metal. (iii) Subsequently, with increasing plating capacity, the deposited Zn progressively fills the internal space of the nanocube framework, achieving a conformal dendrite-free infilling behavior. This study advances the field by designing a uniquely self-reconstructing, stratified interface. Through a single, scalable coating step, we integrate a zincophilic metallic In inner layer with a negatively charged fluoride nanocube outer matrix.

The broad applicability of the NMIF@Zn electrode was further assessed by fabricating and evaluating a full battery, which coupled the modified anode with a self-synthesized MnO_2 cathode. (Figure 5a). The cathode material, fabricated via a hydrothermal method, was identified as pure α-MnO_2 by XRD (Figure S43), with all diffraction peaks matching the standard card (PDF #44-0141). Its morphology, as shown by SEM (Figure S44), comprises nanorods that are several micrometers in length and about 35 nm in width.

The superior reaction kinetics of the NMIF@Zn anode are evidenced by CV measurements at 1 mV s^{-1}, which show smaller voltage gaps between the redox peaks compared to bare Zn (Figure 5b). The reduced polarization is attributed to enhanced electron transfer and diminished kinetic barriers at the reconstructed interface. The galvanostatic discharge-charge (GCD) performance of the NMIF@Zn anode was evaluated over a range of current densities from 0.2 to 2 A g^{-1} (Figure 5c and Figure S45). As summarized in Figure 5d, the NMIF@Zn//MnO_2 battery exhibits a high specific capacity of 342.9 mAh g^{-1} at 0.2 A g^{-1} based on Equation S3. Besides, a substantial capacity of 161.3 mAh g^{-1} is retained at a high current density of 2 A g^{-1}, underscoring its rapid reaction kinetics and excellent reversibility. Moreover, when the current density is restored to 0.2 A g^{-1}, the specific capacity of the NMIF@Zn-based battery recovers to 341.5 mAh g^{-1}. In contrast, the battery with a bare Zn anode delivers significantly lower capacities of only 238.4 and 77.6 mAh g^{-1} at 0.2 and 2 A g^{-1}, respectively. Furthermore, upon returning to 0.2 A g^{-1}, its capacity could only recover to 180.4 mAh g^{-1}. The observed capacity difference primarily stems from the distinct interfacial electrochemical environments created by the different anodes, which significantly affect the initial utilization and reaction kinetics of the MnO_2 cathode. The key lies in the fact that in an aqueous ZIB, the overall battery reaction involves Zn^{2+} shuttling between the anode and cathode. The kinetics and reversibility at the anode/electrolyte interface directly influence the polarization, effective voltage window, and thus the accessible capacity of the cathode during the initial cycles. The bare Zn anode suffers from severe polarization, significant hydrogen evolution, and irregular Zn deposition from the very beginning. This leads to a higher overall cell impedance and a less efficient charge transfer process, which reduces the practical amount of Zn^{2+} that can be reversibly (de)intercalated into/from the MnO_2 cathode within the operating voltage window. Consequently, the initial cathode utilization is lower. In contrast, the NMIF@Zn anode, with its in situ formed stratified interface, establishes a highly reversible and kinetically favorable environment from the first cycle. It features a significantly lower nucleation overpotential, reduced charge transfer resistance, and suppressed side reactions. This optimized interface minimizes overall cell polarization, allowing the MnO_2 cathode to operate more efficiently within its theoretical capacity limits [49, 64]. To further investigate the impact of the initial cycling protocol (charge-first versus discharge-first) on full-cell capacity, the initial GCD profiles under both configurations were analyzed. As shown in Figure S46, the GCD curve obtained under the discharge-first protocol closely matches that of the charge-first protocol in both profile shape and delivered capacity. The negligible difference between the two indicates that the initial step has no significant influence on the system's electrochemical behavior. Furthermore, rate performance was evaluated using the discharge-first protocol and compared with

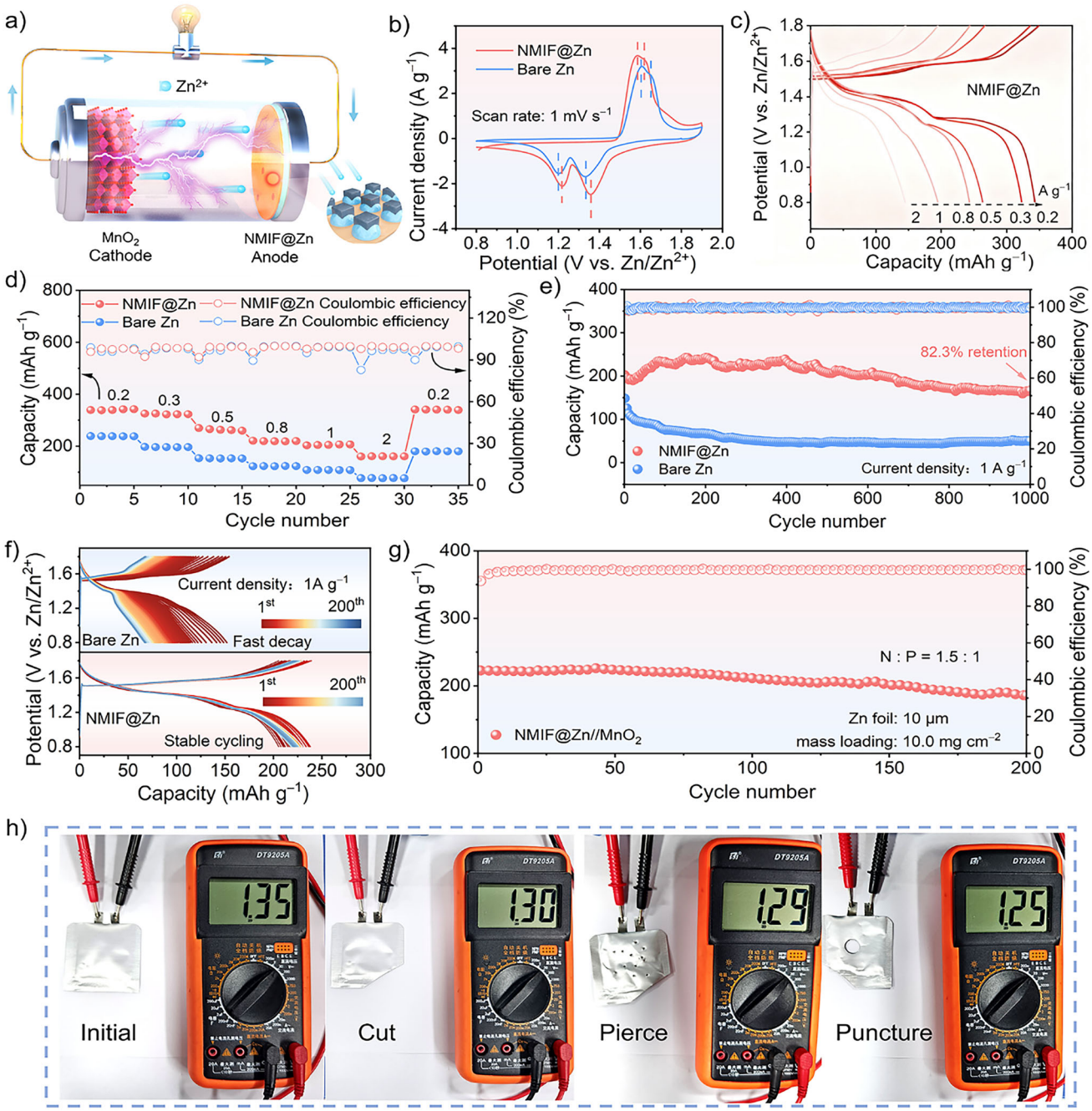

FIGURE 5 | a) Diagram of NMIF@Zn//MnO_2 full battery. b) CV curves of NMIF@Zn//MnO_2 and Zn//MnO_2 batteries at 1 mV s^{-1}. c) GCD profiles of NMIF@Zn//MnO_2 under different current densities. d) Rate performance and e) long-term cycling at 1 A g^{-1} with different anodes. f) Selected GCD profiles of the full batteries. g) Cycling performance at a low N/P capacity ratio of 1.5. h) Open-circuit voltage and safety tests of a pouch cell under destructive conditions, including cutting, piercing, and puncturing.

the previously reported charge-first data (Figure S47). The high consistency observed across various current densities confirms that the sequence of the initial cycling step has a negligible effect on subsequent electrochemical performance. The origin of the outstanding rate performance can be traced to a lower charge-transfer resistance, complemented by a steeper Warburg slope in the low-frequency region that indicates the accelerated interfacial migration of Zn^{2+} ions (Figure S48). Galvanostatic cycling at 1 A g^{-1} was conducted to assess the stability of full batteries (Figure 5e). After 1000 cycles, the battery with the NMIF@Zn anode retains a high specific capacity of 166.8 mAh g^{-1}, corresponding to 82.3% of its initial capacity. This performance is in sharp contrast to that of the battery employing a bare Zn anode, which suffers a significant capacity fade. The pronounced capacity decay in the bare Zn system is directly related to the progressive deactivation of the electrodes upon repeated cycling. There are two distinct initial capacity evolution trends for the two full batteries. For the bare Zn//MnO_2 battery, the anode/electrolyte interface is unstable from the very first cycle. Severe parasitic reactions and non-uniform Zn deposition lead to rapid passivation, continuous consumption of active Zn and electrolyte, and a steep increase in interfacial impedance.

This results in an immediate and steep capacity fade from the beginning of cycling, as the battery's reversibility is compromised from the outset. In contrast, the NMIF@Zn//MnO_2 battery exhibits a more gradual capacity evolution in the initial stage, often characterized by a slight increase or stabilization before reaching a steady state. This behavior is attributed to the in situ activation and self-optimization of the reconstructed NMIF interface. The preferential reduction of In^{3+} to form a metallic In layer and the concomitant enhancement of the surface negative charge on the fluoride nanocubes occur dynamically during the initial plating/stripping cycles. This process progressively refines the interface and optimizes Zn^{2+} transport pathways. Therefore, the initial cycles represent a period of interfacial maturation, leading to an optimized and highly reversible state that supports sustained high capacity [65]. The GCD profiles further reveal that the NMIF@Zn-based full battery exhibits minimal capacity fade over extended cycling (Figure 5f), with virtually no loss in capacity retention. In contrast, the bare Zn system undergoes severe degradation in discharge capacity under identical conditions, which can be mainly ascribed to uncontrolled side reactions at the anode. A stringent full-cell configuration was employed, pairing a high-loading MnO_2 cathode (10.0 mg cm^{-2}) with an ultra-thin Zn foil anode (10 μm) to achieve a low N/P ratio of ~1.5:1. This setup creates intentionally anode-limited conditions. Notably, the NMIF@Zn//MnO_2 full battery under these harsh conditions demonstrates robust cycling stability, retaining 83.4% of its initial capacity after 200 cycles (Figure 5g). This performance confirms that the in situ reconstructed NMIF interface is pivotal in ensuring stable and durable Zn plating/stripping even under high utilization rates of the Zn metal. The effectiveness of the NMIF@Zn electrode in suppressing parasitic reactions was further evaluated by a self-discharge test. After resting a fully charged battery for 24 h, the NMIF@Zn system shows a smaller voltage drop and retains 90.3% of its capacity, markedly higher than the 77.9% retention of the bare Zn system (Figure S49).

The practical applicability of our design was successfully verified using a large-format pouch cell (5 × 5 cm). This single pouch cell exhibits an open-circuit voltage of 1.35 V, which is sufficient to power small electronic devices such as an electric fan (Figure S50). Furthermore, the cell shows outstanding safety under severe mechanical abuse. Even under destructive conditions such as cutting, piercing, or puncturing, it continues to operate, maintaining a consistent open-circuit voltage and underscoring the reliability of the NMIF@Zn anode for real-world applications (Figure 5h). The high cathode-loading pouch cell using the NMIF@Zn anode exhibits an initial discharge capacity of 15.3 mAh at 0.6 A g^{-1} (Figure S51), corresponding to a gravimetric energy density of 295.8 Wh kg^{-1}. This performance was maintained over 50 cycles with 75.1% capacity retention, underscoring the excellent cycling stability and practical viability of the NMIF-modified anode even under realistic conditions. These results clearly indicate that the NMIF@Zn anode is capable of supporting high energy density and outstanding durability.

3 | Conclusion

In summary, an engineered NMIF nanocube interphase was constructed on the Zn anode to guide uniform Zn deposition. This functionality is enabled by an in situ reconfiguration that leverages the synergistic interaction between its components and topology, creating a stratified interface with combined zincophilicity and a negatively charged surface. During plating, a metallic In inner layer forms in situ, providing a zincophilic substrate for guided nucleation. Concurrently, the preferential reduction of In^{3+} enhances the negative charge of the outer fluoride nanocubes, which boosts the interfacial EDLC and directs Zn^{2+} flux through their ordered structure. The synergy between these components facilitates Zn^{2+} conduction and lowers the nucleation overpotential, thereby suppressing dendrite growth and enabling conformal deposition. Benefiting from this synergistic effect, the NMIF@Zn symmetric cells achieve an exceptional cycling lifespan of 2000 h at 3 mA cm^{-2}/3 mAh cm^{-2} and further maintain stable operation at a high DOD of 81.9%. Meanwhile, the asymmetric cells exhibit a high average CE of 99.8% at 1 mA cm^{-2}/1 mAh cm^{-2}, underscoring outstanding durability and reversibility. Furthermore, when paired with a MnO_2 cathode, the full battery demonstrates a high capacity retention rate in a coin-type cell at a low N/P ratio of 1.5, while delivering high energy density in a pouch cell. Collectively, this work demonstrates a viable strategy for the rational design of composite interphases to stabilize Zn metal anodes.

Acknowledgments

The authors appreciate the financial support by the National Natural Science Foundation of China (22272150 and 22502176), Zhejiang Provincial Natural Science Foundation of China (LMS26B030007), and Major Science and Technology Project of Jinhua City (2023-1-060). The calculations were carried out on high performance supercomputer of Zhejiang Normal University.

Conflicts of Interest

The authors declare no conflicts of interest.

Data Availability Statement

Research data are not shared.

References

1. J. N. Hao, S. J. Zhang, H. Wu, L. B. Yuan, K. Davey, and S. Z. Qiao, "Advanced Cathodes for Aqueous Zn Batteries Beyond Zn^{2+} Intercalation," *Chemical Society Reviews* 53 (2024): 4312–4332, https://doi.org/10.1039/D3CS00771E.

2. Y. Dai, R. Lu, C. Zhang, et al., "Zn^{2+}-Mediated Catalysis for Fast-Charging Aqueous Zn-Ion Batteries," *Nature Catalysis* 7 (2024): 776–784, https://doi.org/10.1038/s41929-024-01169-6.

3. H. Wang, W. Ye, B. Yin, et al., "Modulating Cation Migration and Deposition With Xylitol Additive and Oriented Reconstruction of Hydrogen Bonds for Stable Zinc Anodes," *Angewandte Chemie International Edition* 62 (2023): e202218872, https://doi.org/10.1002/anie.202218872.

4. L. E. Blanc, D. Kundu, and L. F. Nazar, "Scientific Challenges for the Implementation of Zn-Ion Batteries," *Joule* 4 (2020): 771–799, https://doi.org/10.1016/j.joule.2020.03.002.

5. J. Wan, R. Wang, Z. Liu, et al., "Hydrated Eutectic Electrolyte Induced Bilayer Interphase for High-Performance Aqueous Zn-Ion Batteries With 100°C Wide-Temperature Range," *Advanced Materials* 36 (2023): 2310623, https://doi.org/10.1002/adma.202310623.

6. H. Lu, B. Yin, T. Zhang, et al., "Dual-Additive Synergistic Complementation Electrolyte Engineering With "Job-Sharing" Modulation

Mechanism for Long-Lifespan Zn-Iodine Batteries," *ACS Applied Materials & Interfaces* 17 (2025): 21234–21245, https://doi.org/10.1021/acsami.5c00459.

7. Y. Chen, B. Yin, Y. Zeng, et al., "Ion-Dipole-Interaction-Manipulated Bilateral Interface Chemistry for Deep Rechargeability and High Redox Activity of Zn-Organic Batteries," *Chem* 11 (2025): 102411, https://doi.org/10.1016/j.chempr.2025.102411.

8. Y. Shao, W. Lu, T. Zhang, et al., "A Self-Recognition Separator for Ion Management to Customize Selective Zn^{2+} Channels Toward Dendrite-Free Zinc Metal Anodes," *Carbon Energy* 7 (2025): e701, https://doi.org/10.1002/cey2.701.

9. J. Luan, H. Yuan, J. Liu, and C. Zhong, "Recent Advances on Charge Storage Mechanisms and Optimization Strategies of Mn-Based Cathode in Zinc–Manganese Oxides Batteries," *Energy Storage Materials* 66 (2024): 103206, https://doi.org/10.1016/j.ensm.2024.103206.

10. S.-J. Yang, L.-L. Zhao, Z.-X. Li, et al., "Achieving Stable Zn Anode via Artificial Interfacial Layers Protection Strategies Toward Aqueous Zn-Ion Batteries," *Coordination Chemistry Reviews* 517 (2024): 216044, https://doi.org/10.1016/j.ccr.2024.216044.

11. M. Tang, Q. Liu, X. Zou, et al., "Engineering In Situ Heterometallic Layer for Robust Zn Electrochemistry in Extreme $Zn(BF_4)_2$ Electrolyte Environment," *Energy Storage Materials* 74 (2024): 103896, https://doi.org/10.1016/j.ensm.2024.103896.

12. M. Peng, Z. Liu, M. Hou, et al., "An Organic-Inorganic-Integrated Solid Electrolyte Interphase With High-Resilience and Anti-Corrosion for Sustainable Zinc Metal Anode," *Angewandte Chemie International Edition* 137 (2025): e202501702, https://doi.org/10.1002/ange.202501702.

13. M. Chen, X. Guo, X. Jiang, et al., "Multi-Group Polymer Coating on Zn Anode for High Overall Conversion Efficiency Photorechargeable Zinc-Ion Batteries," *Angewandte Chemie International Edition* 136 (2024): e202410011, https://doi.org/10.1002/ange.202410011.

14. C. Tian, J. Wang, R. Sun, et al., "Improved Interfacial Ion Migration and Deposition Through the Chain-Liquid Synergistic Effect by a Carboxylated Hydrogel Electrolyte for Stable Zinc Metal Anodes," *Angewandte Chemie International Edition* 135 (2023): e202310970, https://doi.org/10.1002/ange.202310970.

15. X. Xu, S. Li, Z. Cao, S. Yang, and B. Li, "Boosting Ion Diffusion and Charge Transfer by Zincophilic Accordion Arrays to Achieve Ultrafast Aqueous Zinc Metal Batteries," *Advanced Energy Materials* 14 (2024): 2303971, https://doi.org/10.1002/aenm.202303971.

16. X. Liu, J. W. Qian, J. W. Chen, et al., "A Sustainable and Scalable Approach for In Situ Induction of Gradient Nucleation Sites in Biomass-Derived Interface Layers for Ultra-Stable Aqueous Zinc Metal Batteries," *Angewandte Chemie International Edition* 64 (2025): e202504613, https://doi.org/10.1002/anie.202504613.

17. J. Zheng, X. Liu, Y. Zheng, et al., "$Ag_X Zn_y$ Protective Coatings With Selective Zn^{2+} /H^+ Binding Enable Reversible Zn Anodes," *Nano Letters* 23 (2023): 6156–6163, https://doi.org/10.1021/acs.nanolett.3c01706.

18. T. Wang, Q. Xi, K. Yao, et al., "Surface Patterning of Metal Zinc Electrode With an In-Region Zincophilic Interface for High-Rate and Long-Cycle-Life Zinc Metal Anode," *Nano-Micro Letters* 16 (2024): 112, https://doi.org/10.1007/s40820-024-01327-2.

19. X. Liu, Y. Zhang, L. Wang, et al., "Highly Reversible Dendrite-Free Zinc Anode Enabled by a Bilayered Inorganic-Metal Interface Layer," *ACS Nano* 18 (2024): 35325–35335, https://doi.org/10.1021/acsnano.4c11486.

20. P. Cao, X. Zhou, A. Wei, et al., "Fast-Charging and Ultrahigh-Capacity Zinc Metal Anode for High-Performance Aqueous Zinc-Ion Batteries," *Advanced Functional Materials* 31 (2021): 2100398, https://doi.org/10.1002/adfm.202100398.

21. X. Shi, J. Wang, F. Yang, X. Liu, Y. Yu, and X. Lu, "Metallic Zinc Anode Working at 50 and 50 mAh cm^{-2} With High Depth of Discharge via Electrical Double Layer Reconstruction," *Advanced Functional Materials* 33 (2023): 2211917, https://doi.org/10.1002/adfm.202211917.

22. S. Wang, H. Zheng, J. Ding, S. Wu, and S. Fang, "A Coaxial Zinc–Tin Vertically Oriented Array-Based Anode for Achieving Ultrahigh Areal Current and Capacity up to 80 mA cm^{-2} and 80 mA h cm^{-2}," *Journal of Materials Chemistry A* 10 (2022): 1919–1927, https://doi.org/10.1039/D1TA08620K.

23. Y. Zhou, J. Xia, J. Di, et al., "Ultrahigh-Rate Zn Stripping and Plating by Capacitive Charge Carriers Enrichment Boosting Zn-Based Energy Storage," *Advanced Energy Materials* 13 (2023): 2203165, https://doi.org/10.1002/aenm.202203165.

24. F. Yang, C. Tian, L. Bai, et al., "Hierarchical Array Hosts With Concave Spatial Confinement and Zincophilic Seed Mediated Growth for Dendrite-Free Zn Metal Anode," *Composites Part B: Engineering* 301 (2025): 112528, https://doi.org/10.1016/j.compositesb.2025.112528.

25. Z. Wei, G. Qu, Z. Huang, et al., "Gradient Distribution of Zincophilic Sites for Stable Aqueous Zinc-Based Flow Batteries With High Capacity," *Advanced Materials* 36 (2024): 2414388, https://doi.org/10.1002/adma.202414388.

26. Y. Wang, Y. Kong, T. Zhang, C. Chen, H. Wang, and Y. Hu, "Fluorine-Functionalized Chemistry toward Stable Zn Anode in Aqueous Zn-Ion Batteries," *Advanced Energy Materials* 15 (2025): 2502353, https://doi.org/10.1002/aenm.202502353.

27. T. C. Li, C. Lin, M. Luo, et al., "Interfacial Molecule Engineering for Reversible Zn Electrochemistry," *ACS Energy Letters* 8 (2023): 3258–3268, https://doi.org/10.1021/acsenergylett.3c00859.

28. Y. Li, B. Ping, J. Qu, et al., "Constructing Autoregulative Electric Double Layer Through Dielectric Effect Toward Fast Charging Zinc Metal Anode," *Advanced Energy Materials* 15 (2025): 2405804, https://doi.org/10.1002/aenm.202405804.

29. Y. Yang, S. Xu, and Y. He, "Lithium Recycling and Cathode Material Regeneration From Acid Leach Liquor of Spent Lithium-Ion Battery via Facile Co-Extraction and Co-Precipitation Processes," *Waste Management* 64 (2017): 219–227, https://doi.org/10.1016/j.wasman.2017.03.018.

30. R. Qin, Y. Wang, L. Yao, et al., "Progress in Interface Structure and Modification of Zinc Anode for Aqueous Batteries," *Nano Energy* 98 (2022): 107333, https://doi.org/10.1016/j.nanoen.2022.107333.

31. Y. Ai, C. Yang, Z. Yin, et al., "Biomimetic Superstructured Interphase for Aqueous Zinc-Ion Batteries," *Journal of the American Chemical Society* 146 (2024): 15496–15505, https://doi.org/10.1021/jacs.4c03943.

32. Y. Meng, M. Wang, J. Wang, et al., "Robust Bilayer Solid Electrolyte Interphase for Zn Electrode With High Utilization and Efficiency," *Nature Communications* 15 (2024): 8431, https://doi.org/10.1038/s41467-024-52611-z.

33. Z. Xiao, Z. Liu, X. Wu, et al., "Artificial Protrusion Architectures Enabling Horizontal-Diffusion Nucleation for Stable Zinc-Based Batteries," *Journal of the American Chemical Society* 147 (2025): 32216–32224, https://doi.org/10.1021/jacs.5c11951.

34. J. Zheng, Z. Cao, F. Ming, et al., "Preferred Orientation of TiN Coatings Enables Stable Zinc Anodes," *ACS Energy Letters* 7 (2021): 197–203, https://doi.org/10.1021/acsenergylett.1c02299.

35. L. Bin, L. Lixin, L. Tianchen, et al., "Core–Shell Amorphous Carbon-Coated CuZn Powder for Synergistic Protection of Zinc Anodes," *Advanced Energy Materials* 15 (2025): 2405807, https://doi.org/10.1002/aenm.202405807.

36. K. Liu, M. Sun, S. Yang, et al., "Multifunctional Nanodiamond Interfacial Layer for Ultra-Stable Zinc-Metal Anodes," *Advanced Energy Materials* 14 (2024): 2401479, https://doi.org/10.1002/aenm.202401479.

37. W. Huang, D. Yan, Q. Li, et al., "A Chemical Sewing Enabled All-In-One Control Interface for Robust Zinc Metal Anodes," *Advanced Functional Materials* 34 (2024): 2403196, https://doi.org/10.1002/adfm.202403196.

38. J. Wang, J. Peng, W. Huang, et al., "Enabling Stable Zn Anode With PVDF/CNTs Nanocomposites Protective Layer toward High-Performance

Aqueous Zinc-Ion Batteries," *Advanced Functional Materials* 34 (2024): 2316083, https://doi.org/10.1002/adfm.202316083.

39. H. Ke, M. Xiaolin, L. Hongxing, et al., "Nanomagnetism Triggering Carriers Double-Resistance Conduction and Excellent Flexible Thermoelectrics," *Advanced Materials* 37 (2025): 2503046, https://doi.org/10.1002/adma.202414511.

40. T. Chen, F. Huang, Y. Wang, Y. Yang, H. Tian, and J. M. Xue, "Unveiling the Synergistic Effect of Ferroelectric Polarization and Domain Configuration for Reversible Zinc Metal Anodes," *Advancement of Science* 9 (2022): 2105980, https://doi.org/10.1002/advs.202105980.

41. J. Duan, J. Dong, R. Cao, et al., "Regulated Zn Plating and Stripping by a Multifunctional Polymer-Alloy Interphase Layer for Stable Zn Metal Anode," *Advancement of Science* 10 (2023): 2303343, https://doi.org/10.1002/advs.202303343.

42. X. Liu, F. Yang, W. Xu, Y. Zeng, J. He, and X. Lu, "Zeolitic Imidazolate Frameworks as Zn^{2+} Modulation Layers to Enable Dendrite-Free Zn Anodes," *Advancement of Science* 7 (2020): 2002173, https://doi.org/10.1002/advs.202002173.

43. J. Cao, H. Wu, D. Zhang, et al., "In-Situ Ultrafast Construction of Zinc Tungstate Interface Layer for Highly Reversible Zinc Anodes," *Angewandte Chemie International Edition* 63 (2024): e202319661, https://doi.org/10.1002/anie.202319661.

44. S. So, Y. N. Ahn, J. Ko, I. T. Kim, and J. Hur, "Uniform and Oriented Zinc Deposition Induced by Artificial Nb_2O_5 Layer for Highly Reversible Zn Anode in Aqueous Zinc Ion Batteries," *Energy Storage Materials* 52 (2022): 40–51, https://doi.org/10.1016/j.ensm.2022.07.036.

45. G. Qu, Y. Zhao, C. Li, et al., "Hierarchical Interface Enabled by a Guest-Anionic Chemistry for High-Rate Aqueous Zinc-Ion Batteries," *Angewandte Chemie International Edition* 64 (2025): e202422036, https://doi.org/10.1002/anie.202422036.

46. M. Mandl, J. Becherer, D. Kramer, et al., "Sodium Metal Anodes: Deposition and Dissolution Behavior and SEI Formation," *Electrochimica Acta* 354 (2020): 136698, https://doi.org/10.1016/j.electacta.2020.136698.

47. Y. Lu, C.-Z. Zhao, J.-Q. Huang, and Q. Zhang, "The Timescale Identification Decoupling Complicated Kinetic Processes in Lithium Batteries," *Joule* 6 (2022): 1172–1198, https://doi.org/10.1016/j.joule.2022.05.005.

48. Y. Lu, C.-Z. Zhao, R. Zhang, et al., "The Carrier Transition From Li Atoms to Li Vacancies in Solid-State Lithium Alloy Anodes," *Science Advances* 7 (2021): eabi5520, https://doi.org/10.1126/sciadv.abi5520.

49. Q. Zong, B. Lv, C. Liu, et al., "Dendrite-Free and Highly Stable Zn Metal Anode With $BaTiO_3$ /P(VDF-TrFE) Coating," *ACS Energy Letters* 8 (2023): 2886–2896, https://doi.org/10.1021/acsenergylett.3c01017.

50. Z. Wu, Y. Wang, and C. Zhi, "Zinc-Anode Reversibility and Capacity Inflection as an Evaluation Criterion," *Joule* 8 (2024): 2442–2448, https://doi.org/10.1016/j.joule.2024.07.023.

51. J. Li, H. Liang, N. Li, et al., "Regioisomerism-Guided Interfacial Design Toward Stable Zinc Metal Anodes," *Energy & Environmental Science* 18 (2025): 10338–10350, https://doi.org/10.1039/D5EE04705F.

52. Y. Zhong, M. Liu, Y. Lu, et al., "An In-Depth Study of Heterometallic Interface Chemistry: Bi-Component Layer Enables Highly Reversible and Stable Zn Metal Anodes," *Energy Storage Materials* 55 (2023): 575–586, https://doi.org/10.1016/j.ensm.2022.12.024.

53. X. Guo, Q. Peng, K. Shin, et al., "Construction of a Composite Sn-DLC Artificial Protective Layer With Hierarchical Interfacial Coupling Based on Gradient Coating Technology toward Robust Anodes for Zn Metal Batteries," *Advanced Energy Materials* 14 (2024): 2402015, https://doi.org/10.1002/aenm.202402015.

54. G. Wang, Q. Yao, J. Dong, et al., "In Situ Construction of Multifunctional Surface Coatings on Zinc Metal for Advanced Aqueous Zinc–Iodine Batteries," *Advanced Energy Materials* 14 (2024): 2303221, https://doi.org/10.1002/aenm.202303221.

55. Y. Yang, G. Qu, Z. Wei, et al., "Constructing a Fluoride-Ion Tunnel-Structured Interface to Stabilize the Zn Metal Chemistry at 50°C," *Advanced Functional Materials* 34 (2024): 2409950, https://doi.org/10.1002/adfm.202409950.

56. G. Liang, J. Zhu, B. Yan, et al., "Gradient Fluorinated Alloy to Enable Highly Reversible Zn-Metal Anode Chemistry," *Energy & Environmental Science* 15 (2022): 1086–1096, https://doi.org/10.1039/D1EE03749H.

57. Y. Liu, X. Zhang, S. M. Shaaban, et al., "Postpone Interfacial Impoverishment of Zn-Ions via Neodymium-Based Conversion Films for Stable Zn Metal Anodes," *Advanced Energy Materials* 15 (2025): 2500962, https://doi.org/10.1002/aenm.202500962.

58. R. Zhao, J. Yang, X. Han, et al., "Stabilizing Zn Metal Anodes via Cation/Anion Regulation Toward High Energy Density Zn-Ion Batteries," *Advanced Energy Materials* 13 (2023): 2203542, https://doi.org/10.1002/aenm.202203542.

59. H. Tang, N. Hu, L. Ma, et al., "Interfacial Dual-Modulation via Cationic Electrostatic Shielding and Anionic Preferential Adsorption Toward Planar and Reversible Zinc Electrodeposition," *Advanced Functional Materials* 34 (2024): 2402484, https://doi.org/10.1002/adfm.202402484.

60. J. Li, C. Wei, M. Zhao, et al., "In Situ Chemical Construction of Ultrathin Zn^{2+} -Conductive Interphase for Dendrite-Free Zinc Metal Batteries," *Angewandte Chemie International Edition* 137 (2025): e202514671, https://doi.org/10.1002/ange.202514671.

61. L. Wang, B. Zhang, W. Zhou, et al., "Cation-in-Mesopore Complex for 20 Ah-Level Aqueous Battery," *Angewandte Chemie International Edition* 64 (2025): e202501010, https://doi.org/10.1002/anie.202501010.

62. E. McCafferty, "Validation of Corrosion Rates Measured by the Tafel Extrapolation Method," *Corrosion Science* 47 (2005): 3202–3215, https://doi.org/10.1016/j.corsci.2005.05.046.

63. E. V. Dydek, B. Zaltzman, I. Rubinstein, D. S. Deng, A. Mani, and M. Z. Bazant, "Overlimiting Current in a Microchannel," *Physical Review Letters* 107 (2011): 118301, https://doi.org/10.1103/PhysRevLett.107.118301.

64. Q. Hu, X. Wang, J. Cui, et al., "A Three-Tiered Golf Anode Towards Ultralong-Life Zn−Mn Aqueous Batteries," *Angewandte Chemie International Edition* 137 (2025): e202421217, https://doi.org/10.1002/ange.202421217.

65. X. Zeng, K. Xie, S. Liu, et al., "Bio-Inspired Design of an In Situ Multifunctional Polymeric Solid–Electrolyte Interphase for Zn Metal Anode Cycling at 30 mA cm^{-2} and 30 mA h cm^{-2}," *Energy & Environmental Science* 14 (2021): 5947–5957, https://doi.org/10.1039/D1EE01851E.

Supporting Information

Additional supporting information can be found online in the Supporting Information section.

Supporting File 1:: anie71578-sup-0001-SuppMat.doc.